

Article

MEMS Electrostatically Driven Coupled Beam Filter Banks

Richard Syms *  and Adam Bouchaala

Department of Electrical and Electronic Engineering, Imperial College London, Exhibition Road, London SW7 2AZ, UK; a.bouchaala@imperial.ac.uk

* Correspondence: r.syms@imperial.ac.uk; Tel.: +44-207-594-6203

Abstract: MEMS bandpass filters based on electrostatically driven, mechanically coupled beams with in-plane motion have been demonstrated up to the VHF band. Filters higher than second order with parallel plate drives have inherent tuning difficulties, which may be resolved by adding mass-loaded beams to the ends of the array. These beams deflect for DC voltages, and thus allow synchronized electrostatic tuning, but do not respond to in-band AC voltages and hence do not interfere with dynamic synchronization. Additional out-of-band responses may be damped, leaving the desired response. The principle is extended here to close-packed banks of filters, with adjacent arrays sharing mass-loaded beams that localize modes to sub-arrays. The operating principles are explained using a lumped element model (LEM) of the equations of motion in terms of resonant modes and the reflection of acoustic waves at discontinuities. Performance is simulated using the LEM and verified using the more realistic stiffness matrix method (SMM) for banks of up to eight filters. Similar or dissimilar filters may be combined in a compact arrangement, and the method may be extended to higher order resonances and alternative coupled resonator systems.

Keywords: mechanical filter; coupled resonator; MEMS



Citation: Syms, R.; Bouchaala, A. MEMS Electrostatically Driven Coupled Beam Filter Banks. *Micromachines* **2023**, *14*, 2214. <https://doi.org/10.3390/mi14122214>

Academic Editor: Donghwi Lee

Received: 15 November 2023

Revised: 1 December 2023

Accepted: 4 December 2023

Published: 7 December 2023



Copyright: © 2023 by the authors. Licensee MDPI, Basel, Switzerland. This article is an open access article distributed under the terms and conditions of the Creative Commons Attribution (CC BY) license (<https://creativecommons.org/licenses/by/4.0/>).

1. Introduction

Because gas and material damping can be so low, high Q-factors can be obtained from vacuum packaged, electrostatically driven silicon micro-electro-mechanical systems (MEMS) [1–4]. Bandpass filters based on coupled resonators with in-plane linear motion and comb and parallel plate drives have been demonstrated at frequencies from tens of kHz [5–8] to tens of MHz [9–11] for intermediate frequency (IF) filtering [7]. Filter banks have also been proposed for channel selection [12,13] and hearing aids [14]. Filters can be electrostatically tuned [15–19], and mechanical coupling between elements can be replaced by electrostatic coupling [20–22] or a mixture of the two [23,24]. Methods have been developed to fabricate nanoscale coupling elements [25–28] and electrode gaps [29–31], CMOS integration has been demonstrated [32,33], and alternatives to simple linear arrangements have been proposed [34–37]. Reviews can be found in [38,39].

The order of the filter depends on the number of coupled resonators, but filters with more than two resonators and parallel plate drives suffer from a conflict between static and dynamic synchronization [40]. We have previously proposed a solution based on the addition of mass-loaded beams at the ends of the array. These deflect for DC voltages, and therefore allow synchronized electrostatic tuning, but do not respond to in-band AC voltages and hence do not interfere with dynamic synchronization. Out-of-band responses generated by these beams may be damped, leaving a good approximation to the desired response. This approach above may be applied to any filter arrangement with a similar conflict. Its main drawback is its inefficient use of wafer area. Here, we extend the principle to close-packed banks of filters, with adjacent arrays sharing mass-loaded beams in a compact arrangement. In this case, the effect of mass loading is mode localization, previously studied as a side effect of disorder [41,42]. With suitable design, banks of filters may be realized for applications such as channel selection.

The structure of this paper is as follows. In Section 2, we explain the principle of mechanically synchronized filters. In Section 3, we review the development of a lumped element model (LEM) of coupled beam systems from perturbation theory and demonstrate how it may be used to simulate performance. In Section 4, we extend the approach to arrays of similar filters, explaining the operation of the composite array in terms of its resonant modes. In Section 5, we provide an alternative explanation in terms of the reflectivity of mass-loaded beams for travelling acoustic waves. In Section 6, we consider arrays of dissimilar filters and show how mode localization allows the formation of filter banks. In Section 7, we confirm performance using the more realistic stiffness matrix method (SMM) and briefly discuss the possibility of the operation on higher order modes. Conclusions are drawn in Section 8.

2. Electrostatically Driven Coupled Beam Filters

We start by reviewing the design of a single, mechanically synchronized, electrostatically driven coupled beam filter with parallel plate drives, as described in [40].

2.1. Filter Layout

Figure 1a shows a third-order filter, assumed to be fabricated by anisotropic etching and the undercut of a device layer thickness of d . Fixed parts are shown in red and moving parts in blue and cyan, as shown in Figure 1b in a 3D view near the beam roots. The device consists of five suspended built-in beams of length L_0 and width w_0 attached to anchors. Each beam is separated from its neighbors by a distance s and connected by a 45° meander spring of width w_1 attached at x_1 from the beam root. Each beam has its own drive electrode, with an initial electrode gap g_0 . The connections to sources and loads are provided as shown. A DC voltage V_D is applied to all electrodes for tuning. Since the electrostatic forces on the beams are equal, each will deflect without deforming the meander spring, so the gap modifies everywhere to g and the resonant frequency is equally shifted.

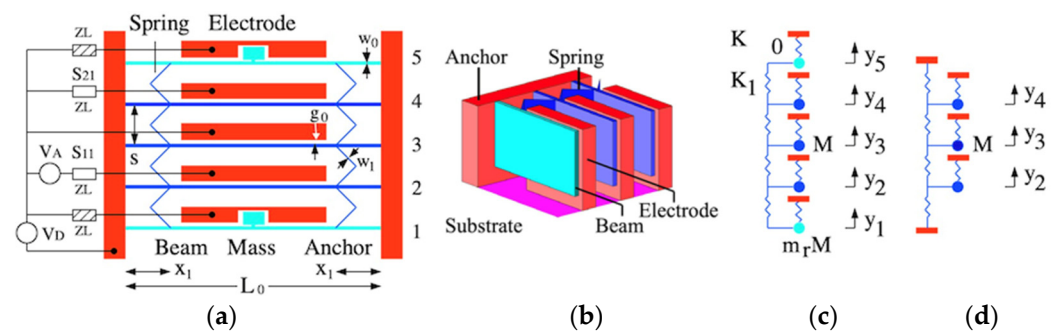


Figure 1. Synchronized third-order filter: (a) layout; (b) 3D view; (c,d) static and dynamic LEMs.

2.2. Mechanical Synchronization

With no electrostatic effects, the inner beams (blue) have identical resonant frequencies based on their own stiffness and that of the meander spring connected on either side. However, because the outer beams are connected to this spring unilaterally, their resonances must be detuned. Although the effect is small, it may spoil a response involving all five beams. Correction may be achieved by modifying the tuning voltages for the outer beams (cyan), but the process is tedious. Instead, these beams are loaded with additional masses at their midpoint, using a short stub connecting each beam to its mass to preserve the design stiffness. Additional electrodes are recessed to allow motion and retain electrostatic uniformity. If the masses are large enough, they can detune these beams so that they cannot participate in collective oscillation near the resonance of the inner beams [40].

The three inner beams comprise the filter, and their number determines its order. Since they behave identically, these beams retain dynamic synchronization. Beam 2 is the input port and is driven by an AC source of voltage V_A with output impedance z_L . Reflection

from this port is described by the scattering parameter S_{11} . Beam 4 is the output port and terminated by a load of impedance z_L . Transmission into this port is described by the scattering parameter S_{21} . Additional loads are provided to damp the motion of the outer beams; for simplicity, these are also z_L . We now show that this arrangement can provide a bandpass response.

3. Lumped Element Model

In this section, we review our own LEM of a coupled beam filter with a parallel plate drive [36,40], giving the main equations for completeness. This model is based on prior work [9] and has been verified using the SMM and a finite element model (COMSOL® 6).

3.1. Modes of a Vibrating Beam

The eigenmodes of an undamped, undriven beam of length L_0 , width w_0 , depth d , density ρ , and Young’s modulus E_0 can be found from the dynamic Euler equation for a built-in beam [43] as follows:

$$Y_v(x) = \left(\frac{\gamma}{\sqrt{L_0}} \right) \left\{ \frac{\sin(\beta_v x) - \sinh(\beta_v x)}{\sin(\beta_v L_0) - \sinh(\beta_v L_0)} - \frac{\cos(\beta_v x) - \cosh(\beta_v x)}{\cos(\beta_v L_0) - \cosh(\beta_v L_0)} \right\} \quad (1)$$

Here, $Y_v(x)$ is the transverse displacement and x is the position along the beam. The eigenvalues β_v are related to the resonant frequencies ω_v by $\beta_v^4 = \omega_v \rho A_0 / E_0 I_0$, where $A_0 = w_0 d$ is the cross-sectional area of the beam and $I_0 = w_0^3 d / 12$ is its second moment of area. The constant γ is chosen so that $\int_0^{L_0} Y_v^2 dx = 1$ and the eigenvalues satisfy the equation $\cos(\beta_v L_0) \cosh(\beta_v L_0) = 1$. For the lowest order mode, the solution is $\beta_1 L_0 = \sqrt{22.37}$. In use, the beam is subjected to a force f and distributed damping r per unit length.

3.2. Lumped Element Model

Figure 1c shows the lumped element model in which each resonator except the first and the last is a mass M supported on a spring of stiffness K_0 . Equivalence with the distributed model is established using factors $\eta_1 = \frac{\text{avg}(Y_1)}{\max(Y_1)} = 0.523$ and $\eta_2 = \frac{\text{avg}(Y_1^2)}{\max(Y_1^2)} = 0.396$ which allow M , K_0 , the damping coefficient R , and force F to be found as follows [9]:

$$M = \rho A_0 L_0 \eta_2, K_0 = \omega_1^2 M, R = r L_0 \eta_2, F = f L_0 \eta_1 \quad (2)$$

For the outer elements, the mass is increased to $m_r M$, where $m_r = (M + \Delta M) / M$ is a mass ratio and ΔM is an additional mass.

3.3. Perturbation Theory

The coupling springs are formed from thinner elements of length L_1 , width w_1 , depth d , density ρ , and Young’s modulus E_1 , inclined at 45° to give a separation $s = L_1 \sqrt{2}$ between the beams. The equivalent spring constant and mass of each pair are $k_1 = 24 E_1 I_1 / L_1^3$ and $m_1 = 2 \rho A_1 L_1$, where $I_1 = w_1^3 d / 12$ and $A_1 = w_1 d$. Here, a different elastic modulus E_1 is introduced for generality, and the mass m_1 is half of the actual mass, to model the motion of mass centers. Perturbation theory [44] allows an equivalent lumped element coupling stiffness K_1 to be found as follows:

$$K_1 = (k_1 - \omega_1^2 m_1) L_0 Y_1^2(x_1) \eta_2 \quad (3)$$

For very small springs, the effect of the mass m_1 may be ignored, and the coupling stiffness then depends on the strength and positions of the springs.

3.4. Electrostatic Transducers

To model electrostatic transducers, we follow [9] and assume that the electrodes act as parallel plate capacitors with capacitance as follows:

$$C = \varepsilon_0 L_0 d / (g_0 - y_D) \quad (4)$$

Here, g_0 is the initial gap and y_D is the static displacement. Application of a DC voltage V_D generates a static force as follows:

$$F_D = \frac{1}{2} C' V_D^2 \eta_1 \quad (5)$$

Here, $C' = \varepsilon_0 L_0 d / (g_0 - y_D)^2$ is the derivative of C . Static equilibrium implies that $F_D = K_{0e} y_D$. Here, $K_{0e} \approx K_0$ is the effective stiffness. This is a snap-down problem [45], leading to a cubic equation whose solution allows C , C' , and the second derivative C'' to be found. If an AC voltage V_A is applied from a source with output impedance z_L , the result is an AC force F_A , a reduction in stiffness ΔK , and an effective load Z_L , given by the following:

$$F_A = V_D C' \eta_1 V_A, \Delta K = \frac{1}{2} V_D^2 C'' \eta_2, Z_L = (V_D C' \eta_1)^2 z_L \quad (6)$$

In general, the characteristic impedance Z_0 of a coupled beam array is complex, but for an infinite lossless array at resonance, it has the real value as follows:

$$Z_{0R} = K_1 / \omega_{1e} \quad (7)$$

Here, $\omega_0 = \sqrt{\left(\frac{K'_0 + 2K_1}{M}\right)}$ is the effective angular resonant frequency, and $K'_0 = K_0 - \Delta K$. Matching is achieved by choosing $Z_L = Z_{0R}$. This requires the load resistance z_L to satisfy $K_v^2 z_L = Z_{0R}$, where $K_v = V_D C' \eta_1$. Very large values of z_L are needed if K_v is small, so electrode gaps must be small to achieve realistic values [9].

3.5. Equations of Motion

Early modeling was carried out using equivalent circuits (see e.g., [6–9]). However, mass loading can be more easily understood with mechanical models. Ignoring the shaded loads, the equations of motion for a five-beam array with ports at $n = 2$ and $n = 4$ and a harmonic drive $F = F_0 \exp(j\omega t)$ at angular frequency ω are as follows [40]:

$$\begin{aligned} \left\{ K'_0 + K_1 - m_r M \omega^2 + j\omega R \right\} y_1 - K_1 y_2 &= 0 \\ \left\{ K'_0 + 2K_1 - M \omega^2 + j\omega(R + Z_L) \right\} y_2 - K_1 (y_1 + y_3) &= F_0 \\ \left\{ K'_0 + 2K_1 - M \omega^2 + j\omega R \right\} y_3 - K_1 (y_2 + y_4) &= 0 \\ \left\{ K'_0 + 2K_1 - M \omega^2 + j\omega(R + Z_L) \right\} y_4 - K_1 (y_3 + y_5) &= 0 \\ \left\{ K'_0 + K_1 - m_r M \omega^2 + j\omega R \right\} y_5 - K_1 y_4 &= 0 \end{aligned} \quad (8)$$

The displacements y_n can be found by elimination, and reflection and transmission scattering parameters S_{11} and S_{21} extracted by standard methods.

3.6. Example Response

Simulations were carried out for the dimensions in Table 1, which models arrays of weakly coupled beams resonant near 1 MHz. The material parameters in Table 2 were used

to model devices in (100) Si with the main and coupling beams in the $\langle 110 \rangle$ and $\langle 010 \rangle$ directions [46]. A quality factor of $Q = \omega_0 M/R = 5000$ was taken as representative of vacuum packaging; however, its value is unimportant, provided that it is large. A mass ratio $m_r = 1.5$ was assumed for mass-loaded beams.

Table 1. Layout parameters used in the LEM simulation.

L_0	w_0	d	$\alpha = x_1/L_0$	s	w_1	g_0
(μm)	(μm)	(μm)		(μm)	(μm)	(μm)
150	3	4	0.25	8	0.1	0.1

Table 2. Material and other parameters used in the LEM simulation.

ρ	E_0	E_1	V_D	z_L	Q	m_r
(kg/m^3)	(N/m^2)	(N/m^2)	(V)	($\text{k}\Omega$)		
2332	169×10^9	130×10^9	2.72	207	5000	1.5

The DC voltage V_D was first applied to achieve resonance at 1 MHz. An AC voltage of amplitude $V_A = 0.1$ mV was then applied at the input port and the load impedance was adjusted for matching. Figure 2a shows the variation of the S-parameters with frequency. The response is bandpass, with correct tuning and matching at the design frequency (dotted line), but a transmission spike can be seen due to end-beam motion. Figure 2b shows the results with the shaded loads in Figure 1a damping this motion. The response is now purely bandpass, and the dynamic model has reduced to Figure 1d.

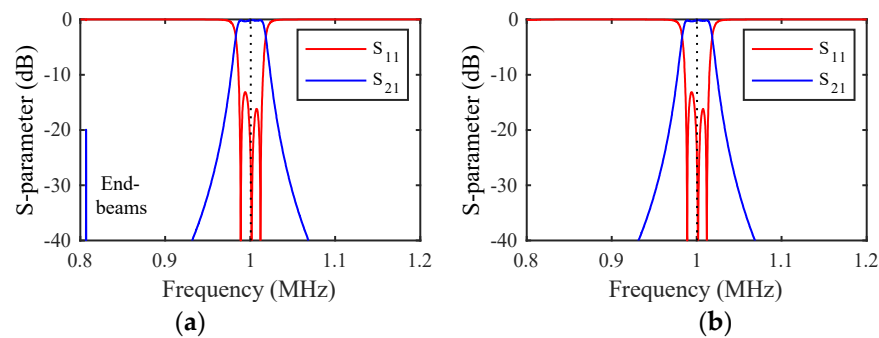


Figure 2. Frequency response of a third-order filter (a) without and (b) with end-beam damping, LEM.

4. Filter Bank—Similar Filters

In this section, we consider how the mass-loading principle can be extended to a larger array capable of acting as a bank of filters which are initially similar.

4.1. Filter Bank

Figure 3a shows an example array containing nine beams, where mass loading (cyan) has been applied to the central beam 5 as well as the end beams 1 and 9. Two sets of three beams (blue) then remain to act as similar third-order filters 1 and 2, separated by a common mass-loaded beam. This arrangement improves wafer utilization by eliminating the need for die separation and (as we show later) can be extended to dissimilar filters. The input and output ports of filter 1 are 1 and 2, while those of filter 2 are 3 and 4.

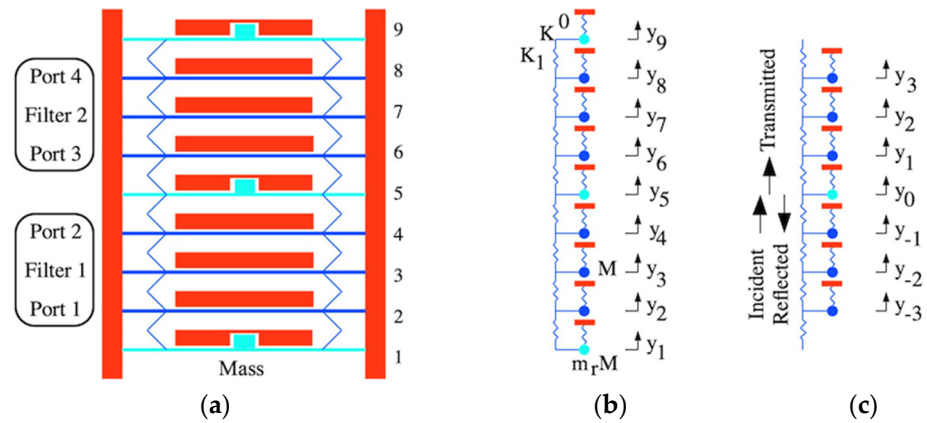


Figure 3. Bank of identical third-order filters: (a) layout; (b) LEM; (c) LEM for infinite array with defect.

Electrical connections are omitted for simplicity but are analogous to those in Figure 1a. DC voltages V_D must be applied to each electrode and AC voltages V_{A1} and V_{A2} to the two input ports 1 and 3, using sources with impedance z_L . Similarly, the two output ports 2 and 4 must be connected to loads, and the mass-loaded beams should again be damped. The scattering parameters of filter 1 are S_{11} and S_{21} , while those of filter 2 are S_{33} and S_{43} . The design supports global electrostatic tuning but not the tuning of individual filters; this would involve compression or extension of the meander springs near the central beam, which would then be relaxed by the springs elsewhere.

4.2. Equations of Motion

The lumped element equivalent of this arrangement is shown in Figure 3b. Omitting damping on the mass-loaded beams to begin with, the equations of motion for harmonic drives $F_A = F_{0A} \exp(j\omega t)$ and $F_B = F_{0B} \exp(j\omega t)$ are as follows:

$$\begin{aligned}
 \{K'_0 + K_1 - m_r M \omega^2 + j\omega R\} y_1 - K_1 y_2 &= 0 \\
 \{K'_0 + 2K_1 - M \omega^2 + j\omega(R + Z_L)\} y_2 - K_1(y_1 + y_3) &= F_{0A} \\
 \{K'_0 + 2K_1 - M \omega^2 + j\omega R\} y_3 - K_1(y_2 + y_4) &= 0 \\
 \{K'_0 + 2K_1 - M \omega^2 + j\omega(R + Z_L)\} y_4 - K_1(y_3 + y_5) &= 0 \\
 \{K'_0 + 2K_1 - m_r M \omega^2 + j\omega R\} y_5 - K_1(y_4 + y_6) &= 0 \\
 \{K'_0 + 2K_1 - M \omega^2 + j\omega(R + Z_L)\} y_6 - K_1(y_5 + y_7) &= F_{0B} \\
 \{K'_0 + 2K_1 - M \omega^2 + j\omega R\} y_7 - K_1(y_6 + y_8) &= 0 \\
 \{K'_0 + 2K_1 - M \omega^2 + j\omega(R + Z_L)\} y_8 - K_1(y_7 + y_9) &= 0 \\
 \{K'_0 + K_1 - m_r M \omega^2 + j\omega R\} y_9 - K_1 y_8 &= 0
 \end{aligned} \tag{9}$$

These equations can be solved as before, but we first focus on the resonant modes.

4.3. Eigenmodes

In the absence of damping and driving forces, Equation (9) reduces to the following:

$$\begin{aligned}
 (\omega_2^2 - \omega^2)y_1 - \kappa_m y_2 &= 0 \\
 (\omega_0^2 - \omega^2)y_2 - \kappa(y_1 + y_3) &= 0 \\
 (\omega_0^2 - \omega^2)y_3 - \kappa(y_2 + y_4) &= 0 \\
 (\omega_0^2 - \omega^2)y_4 - \kappa(y_3 + y_5) &= 0 \\
 (\omega_1^2 - \omega^2)y_5 - \kappa_m(y_4 + y_6) &= 0 \\
 (\omega_0^2 - \omega^2)y_6 - \kappa(y_5 + y_7) &= 0 \\
 (\omega_0^2 - \omega^2)y_7 - \kappa(y_6 + y_8) &= 0 \\
 (\omega_0^2 - \omega^2)y_8 - \kappa(y_7 + y_9) &= 0 \\
 (\omega_2^2 - \omega^2)y_9 - \kappa_m y_8 &= 0
 \end{aligned} \tag{10}$$

Here, further resonant frequencies are defined as $\omega_1^2 = (K'_0 + 2K_1)/m_r M$ and $\omega_2^2 = (K'_0 + K_1)/m_r M$, and new coupling terms are given by $\kappa = K_1/M$ and $\kappa_m = K_1/(m_r M)$.

For characteristic modes oscillating at the μ th angular resonant frequency ω_μ , we may write $y_{\mu n} = Y_{\mu n} \exp(j\omega_\mu t)$, where the constants $Y_{\mu n}$ define the overall mode shapes. The resonant frequencies are the eigenvalues of the tridiagonal matrix \underline{M} , given by the following:

$$\underline{M} = \begin{pmatrix} \omega_2^2 & -\kappa_m & 0 & 0 & 0 & 0 & 0 & 0 & 0 \\ -\kappa & \omega_0^2 & -\kappa & 0 & 0 & 0 & 0 & 0 & 0 \\ 0 & -\kappa & \omega_0^2 & -\kappa & 0 & 0 & 0 & 0 & 0 \\ 0 & 0 & -\kappa & \omega_0^2 & -\kappa & 0 & 0 & 0 & 0 \\ 0 & 0 & 0 & -\kappa_m & \omega_1^2 & -\kappa_m & 0 & 0 & 0 \\ 0 & 0 & 0 & 0 & -\kappa & \omega_0^2 & -\kappa & 0 & 0 \\ 0 & 0 & 0 & 0 & 0 & -\kappa & \omega_0^2 & -\kappa & 0 \\ 0 & 0 & 0 & 0 & 0 & 0 & -\kappa & \omega_0^2 & -\kappa \\ 0 & 0 & 0 & 0 & 0 & 0 & 0 & -\kappa_m & \omega_2^2 \end{pmatrix} \tag{11}$$

Figure 4a shows the variation of the normalized frequencies ω_μ/ω_0 with the mass ratio m_r for the example stiffness ratio $K_1/K'_0 = 0.0244$ obtained using the parameters of Tables 1 and 2. The results fall into two groups, each containing distinct values when $m_r = 0$. The upper band (blue) represents modes involving motion of the filter beams. The width of this band depends on K_1/K'_0 , which ultimately determines the filter bandwidth. For typical applications, this ratio must be small, implying that the width of the coupling spring must be small compared with that of the main beams. As m_r increases, each pair of resonances degenerates to a constant value. The lower group (cyan) contains modes of the mass-loaded beams. As m_r increases, two of these resonances (symmetric and antisymmetric modes of the end beams) again degenerate, while the third (involving the central beam) remains slightly higher and the group separates further from the main band.

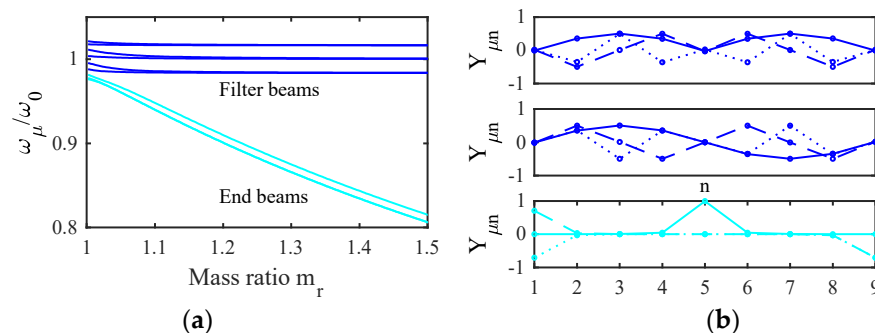


Figure 4. A two-filter bank: (a) variation of resonant frequency with m_r , (b) mode shapes with $m_r = 1.5$.

Figure 4b shows the corresponding mode shapes for $m_r = 1.5$. The two upper plots show that the blue resonances are collective symmetric and antisymmetric modes with zeros at the ends and center of the array. In this case, there is no mode localization, and the injection of a signal into either filter must excite both sets of modes together. However, the modes may then add in one filter and cancel in the other to give the appearance of excitation of a single filter. Numerical analysis shows that effective cancellation merely requires a sufficiently large value of m_r . The lower plot confirms that the cyan resonances in Figure 4a involve the loaded beams alone. Consequently, for large m_r , there will be no motion of these beams except near discrete out-of-band frequencies.

4.4. Example Response

Figure 5a shows the frequency variation of the S-parameters of filter 1 for the parameters of the previous section and $m_r = 1.5$, assuming that the mass-loaded beams are damped. The response is essentially that of Figure 2b, a bandpass response. The responses obtained when filter 2 is excited are similar, implying that independent operation of the two filters has been achieved. However, because the filters are coupled together, there is some potential for crosstalk. Figure 5b shows the frequency variation of the outputs from filter 2. The unwanted outputs are everywhere below ~ -30 dB and can be suppressed further by increasing m_r . However, it should be noted that there are limits on the achievable value of m_r due to the finite space occupied by the loading elements.

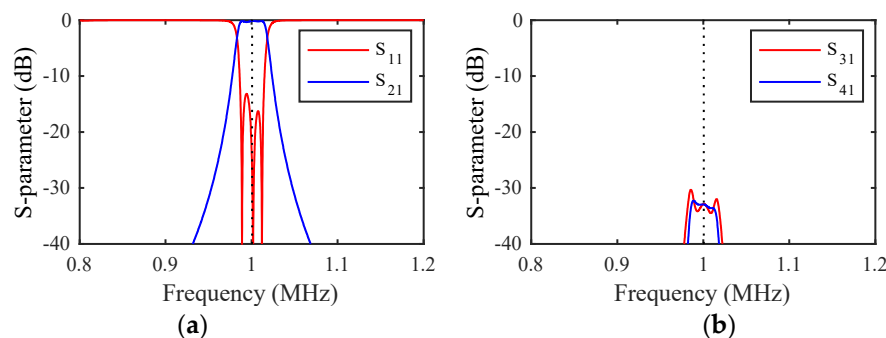


Figure 5. S-parameter variations with filter 1 excited: outputs from (a) filter 1 and (b) filter 2. LEM.

5. Mass-Loaded Beams as Reflectors

We now provide an explanation for the subdivision of the array by considering mass-loaded beams as reflectors for travelling acoustic waves.

5.1. Dispersion Equation for Acoustic Waves

We first consider an infinite line of identical coupled beams with resonant frequency ω_0 and coupling constant κ . In the absence of loss, the equations of motion are as follows:

$$(\omega_0^2 - \omega^2)y_n - \kappa(y_{n-1} + y_{n+1}) = 0 \tag{12}$$

In the uniform regions, we may assume travelling wave solutions in the following form:

$$y_n = y_0 \exp(-jnka) \tag{13}$$

Here, y_0 is the wave amplitude, k is the propagation constant, and a is the spacing between resonators. Substituting into Equation (14), we obtain the following dispersion equation:

$$\omega^2 = \omega_0^2 - 2\kappa \cos(ka) \tag{14}$$

Figure 6a shows the dispersion characteristic, assuming $K_1/K_0 = 0.0244$ as before. The variation is essentially that of an acoustic slow-wave structure, and propagation is allowed only over a finite band of frequencies. The addition of loss will introduce a complex propagation constant, so waves decay as they propagate, and allow out-of-band propagation near the band edges; however, the effect will be small with high Q-factors.

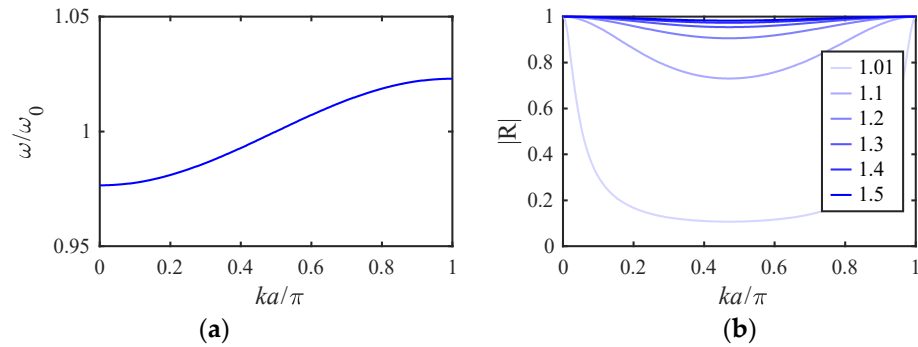


Figure 6. Infinite array: (a) dispersion and (b) variation of $|R|$ with ka at reflectors with different m_r .

5.2. Transmission and Reflection at a Discontinuity

We now assume that there is a perturbation in one beam, which for simplicity we take as beam zero as in Figure 3c. Here, the resonant frequency and coupling are modified to $\omega_1 = \omega_0 / \sqrt{m_r}$ and $\kappa_m = \kappa / m_r$. Near this point, the equations modify to the following:

$$(\omega_0^2 - \omega^2)y_{-1} - \kappa(y_{-2} + y_0) = 0$$

$$(\omega_1^2 - \omega^2)y_0 - \kappa_m(y_{-1} + y_{+1}) = 0 \tag{15}$$

We assume that an upward travelling wave is incident on the discontinuity. Standard physics suggests that this wave will be scattered into reflected and transmitted waves, so we assume solutions in the form of appropriate travelling wave terms:

$$y_n = y_I \exp(-jnka) + y_R \exp(+jnka) \quad n < 0$$

$$y_n = y_T \exp(-jnka) \quad n \geq 0 \tag{16}$$

Here, y_I , y_R , and y_T are the amplitudes of the incident reflected and transmitted waves, respectively. Substituting into Equation (15) and making use of Equation (14), the reflection and transmission coefficients $R = y_R/y_I$ and $T = y_T/y_I$ can be found as follows:

$$R = -\frac{\omega_1^2 - \omega_0^2 + 2(\kappa - \kappa_m) \cos(ka)}{\omega_1^2 - \omega_0^2 + 2(\kappa - \kappa_m) \cos(ka) + 2j\kappa_m \sin(ka)} \tag{17}$$

$$T = \frac{2j\kappa_m \sin(ka)}{\omega_1^2 - \omega_0^2 + 2(\kappa - \kappa_m) \cos(ka) + 2j\kappa_m \sin(ka)} \tag{18}$$

Since $|R|^2 + |T|^2 = 1$, these equations conserve power, and they satisfy the standard relations $T = 1 + R$ and reduce to $R = 0$ and $T = 1$ when $m_r = 1$. Figure 6b shows the variation of $|R|$ for the same parameters as Figure 6a and different values of m_r . The reflectivity varies across the band, with $R = -1$ at the band edges when $ka = 0$ or $ka = \pi$ and the smallest effect near the band center. However, as m_r rises, $R \rightarrow -1$ over the entire band and the loaded beam acts as a mirror for acoustic waves. Thus, mass loading can be understood in terms of reflectors that divide an array into independent sub-arrays.

6. Filter Bank—Dissimilar Filters

We now consider how mass loading can create banks of dissimilar filters, differing in their order or their center frequency (or both). In either case, mode localization occurs.

6.1. Dissimilar Orders

For example, Figure 7a shows a 10-beam array subdivided into third-order (blue) and fourth-order (green) filters using mass-loaded beams (cyan). The coupled equations can be developed as before and then reduced to an eigenvalue–eigenvector problem.

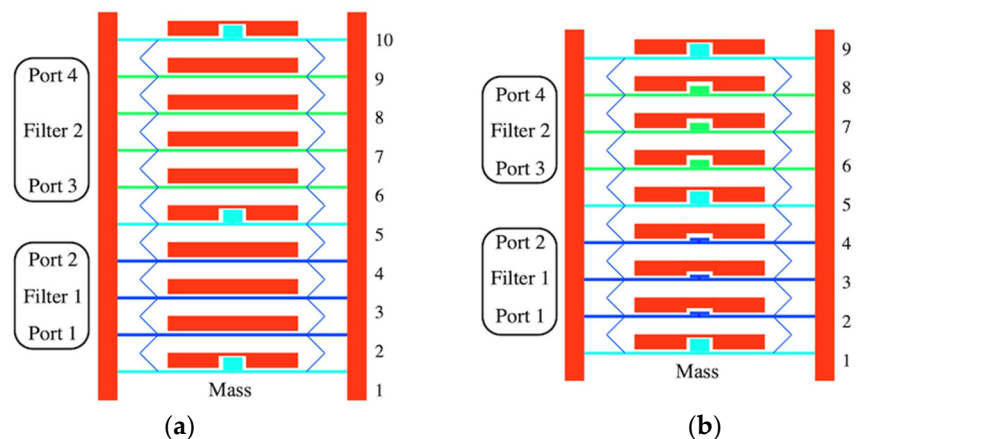


Figure 7. Banks of non-identical filters: (a) dissimilar order and (b) dissimilar frequency.

Figure 8a shows the variation of the normalized resonant frequencies ω_μ/ω_0 with m_r for the previous parameters. The filter resonances again stabilise as m_r increases but now form superimposed three-mode (blue) and four-mode (green) bands. A further group (cyan) involving the end beams again gradually diverges. Figure 8b shows the mode shapes for $m_r = 1.5$, showing that the main modes are now localized to the two filters. In contrast to the previous section, the operation of a single filter now involves a subset of modes, and no cancellation is involved. Figure 9a,b show the frequency dependence of the S-parameters for the two filters. In each case, tuning and matching are correct and a bandpass response is obtained; however, the filter responses are clearly of different order.

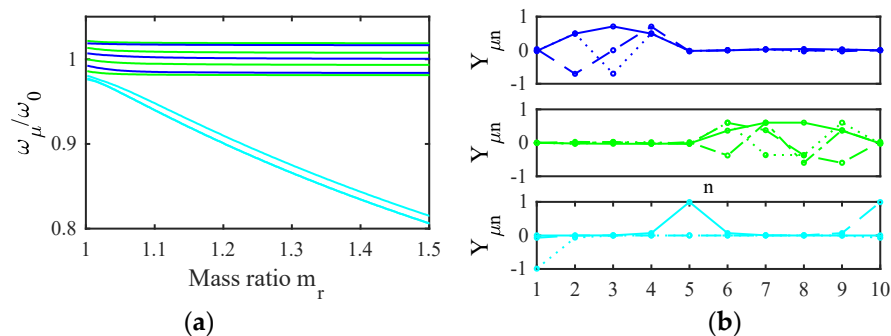


Figure 8. Filters of dissimilar order: (a) variation of ω_μ with m_r ; (b) eigenmodes for $m_r = 1.5$.

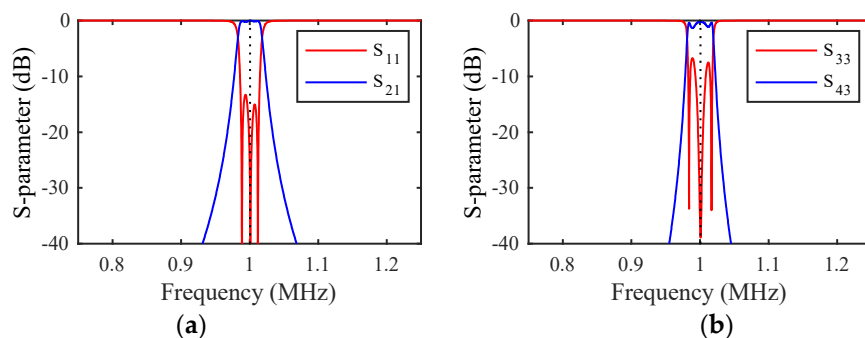


Figure 9. Filters of dissimilar order: response of (a) filter 1 and (b) filter 2. LEM.

6.2. Dissimilar Frequencies

The principle may be extended to dissimilar center frequencies. For example, Figure 7b shows a nine-element array subdivided into two third-order filters (blue and green) using mass-loaded beams (cyan). The port arrangements are unchanged, but the filter elements are now also mass loaded to tune their resonant frequency, using equivalent masses $m_{r1}M$ and $m_{r2}M$. If the two mass ratios are written in the form $m_{ri} = 1 + \Delta m_{ri}$, we would expect the corresponding center frequencies ω_{0i} to scale as follows:

$$\omega_{0i} \propto \frac{1}{\sqrt{m_{ri}}} \approx 1 - \frac{\Delta m_{ri}}{2} \tag{19}$$

This approximation allows suitable values of m_{ri} to be estimated; further correction can then be used to space the center frequencies more accurately. Figure 10a shows the variation of the normalized resonant frequencies ω_μ/ω_0 with m_r , assuming the same parameters and $m_{r1} = 1$, $m_{r2} = 1.1$, for which the normalised resonant frequencies can be estimated as 1 and 0.95. The resonances now fall into separate bands corresponding to motion in filters 1 (blue) and 2 (green) and a further group involving the end beams (cyan). As before, the filter resonances stabilise when m_r is large. Figure 10b shows the mode shapes with $m_r = 1.5$ which confirm that the main modes are again localized.

Figure 11a shows the frequency dependence of transmission for each filter, with V_D adjusted to center the response around 1 MHz and to the load resistors altered to improve matching; these must be scaled as $z_{Li} = z_L \sqrt{m_{ri}}$. Here, '1' denotes the transmission of filter 1, and so on. In each case, a bandpass response is obtained, but the center frequencies are up- and down-shifted, implying that the array has provided two different filters.

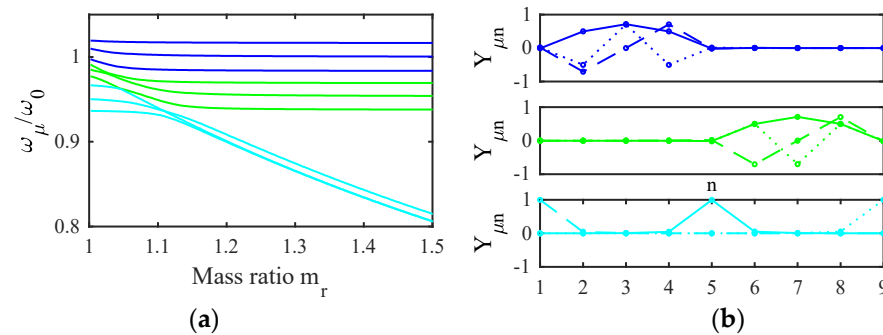


Figure 10. Filters of dissimilar frequency: (a) variation of ω_μ with m_r ; (b) eigenmodes for $m_r = 1.5$.

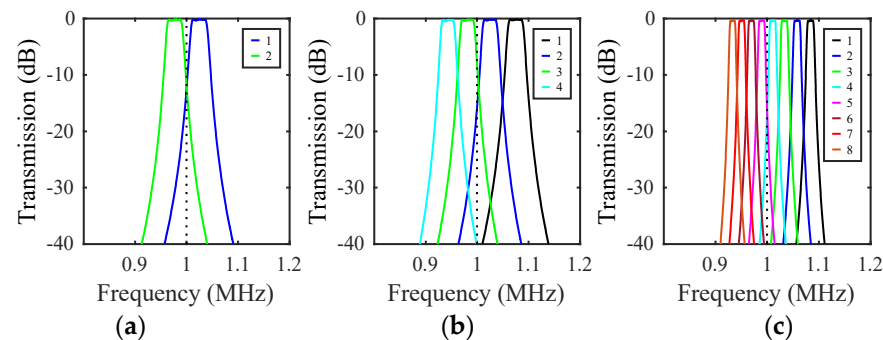


Figure 11. Frequency dependence of transmission for banks of (a) 2, (b) 4, and (c) 8 filters. LEM.

6.3. Filter Banks

The unoccupied frequency interval between the green and cyan resonances in Figure 10a suggests that the mass-loading principle may be extended to larger filter banks. This is indeed the case, as all that is required is that the center frequencies are equally spaced and the bands do not overlap with each other or with the resonances of the mass-loaded beams. At minimum, this requires that mass ratio m_{ri} of the i th filter be chosen so that $m_{r1} = 1$, $m_{ri} > m_{ri-1}$, and $m_{ri} < m_r$. For the parameters here, four filters may be realised. Figure 11b shows the results obtained by mass loading the arrays so that $m_{ri} = 1 + 0.1(i - 1)$ and $m_r = 1.5$, and again adjusting V_D and load resistors to center the response and improve matching. A set of four near-identical frequency-shifted responses is now obtained in the format needed for a channel selector or multiplexer.

The maximum number of channels depends on the filter bandwidth. For the parameters here, similar results can be obtained for eight filters provided that their bandwidth is reduced to avoid channel overlap by weakening the coupling springs, choosing suitable mass ratios, and adjusting tuning and matching. Figure 11c shows the results obtained by increasing the separation s to $10 \mu\text{m}$ and using the mass ratios $m_{ri} = 1 + 0.05(i - 1)$ and $m_r = 1.5$. Eight near-identical responses are obtained. The overall bandwidth may itself be raised by increasing m_r . In practice, there are limits set by the physical size of the masses; we discuss this further in Section 7.

7. Stiffness Matrix Method

Distributed devices can be simulated using the finite element method (FEM) [47] and the stiffness matrix method [48]. The FEM solves partial differential equations with boundary conditions by subdividing space into a mesh and reducing the problem to a system of nodal equations. It can provide accurate models of MEMS involving different physical domains, but calculations are extremely lengthy for high-aspect-ratio sub-spaces when the number of nodes is large [49]. The SMM replaces flexible elements with equivalent stiffness terms from the Euler beam bending theory [43], and electrostatic transducers with analytic approximations [50]. The result is again simultaneous equations, but their number is greatly reduced. Both methods allow the exploration of realistic layouts, without

assuming responses involve specific modes. To avoid excessive run times associated with large coupled-beam arrays using FEM, we focus here on the SMM.

7.1. SMM Solver

Two-dimensional SMM calculations were performed using a Matlab® R2020a model previously verified against FEM [36,40]. The stiffness matrix \mathbf{K} was constructed from the layout, dimensions, and material parameters, with E_0 reduced to model electrostatic detuning. Long beams were divided into 16 sections to improve accuracy. Axial, transverse, and angular displacements at nodes were found for a vector of applied forces and torques.

Dynamic analysis was performed using additional mass and damping matrices. The mass matrix \mathbf{M} was formed by combining dimensions and densities with standard relations for motions of centers of mass. The damping matrix \mathbf{C} was modeled using Rayleigh's method as $\mathbf{R} = a\mathbf{M} + b\mathbf{K}$ [43]. Here, a and b are mass and spring damping coefficients, with a determined from the Q -factor and b set to zero. Ports were simulated by increasing the damping for these beams, using a damping coefficient determined from the load impedance. Assuming harmonic forces and displacements as $(\mathbf{F}, \mathbf{U}) e^{j\omega t}$, substitution into the governing equation yields $(\mathbf{K} - \omega^2\mathbf{M} + j\omega\mathbf{R})\mathbf{U} = \mathbf{F}$. This equation was solved by matrix inversion, and the velocity vector was constructed as $\mathbf{S} = j\omega\mathbf{U}$. The scattering parameters were then extracted from midpoint velocities.

7.2. Physical Layouts

Simulations were carried out for the parameters in Tables 1 and 2. For example, Figure 12a shows the statically deflected shape of an array containing two unloaded three-element sub-arrays, as in Figure 3a. Here, thick horizontal lines represent the main beams and thin inclined lines represent the meander springs. Anchors and drive electrodes are not shown. The beams are loaded with masses on elements 1, 5, and 9. The short stub connecting each beam to its mass is omitted, as it will have no effect in a SMM model.

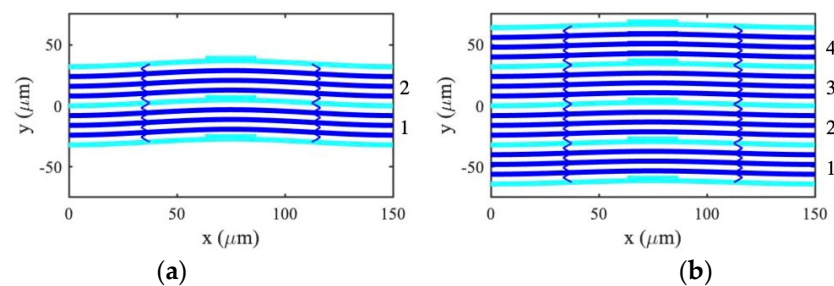


Figure 12. Layout and deflected shape of banks of (a) 2 and (b) 4 filters. SMM.

The physical size of the masses illustrates the main limitation. Here, a mass ratio $m_r = 1.5$ is achieved using a mass measuring $4 \mu\text{m} \times 22.5 \mu\text{m}$; larger masses will consume a greater fraction of the space allocated to electrodes, and care will be needed to ensure electrostatic uniformity. The beams deflect identically as expected.

7.3. Mode Synchronization

Figure 13a shows the variation of the normalized eigenfrequencies with mass ratio m_r . This figure should be compared with earlier results from the LEM in Figure 4a; the qualitative agreement is excellent, and the modes synchronize correctly as m_r rises. Minor differences can be ascribed to the approximations inherent in perturbation theory. Figure 13b shows a similar variation over an enlarged frequency range to illustrate the effect of higher order modes. The resonances of the first-order (symmetric) modes lie at the bottom of the plot. A second group of resonances lie at the center; these correspond to second-order (antisymmetric) modes. Since their mode shapes have zeros at the point of mass loading, there can be no variation in their resonances with m_r . A third group lie at the top; these involve third-order symmetric modes. This group is also synchronized as m_r rises. These

results confirm that basic behaviour is captured well by the LEM but admit the possibility of operating on higher order symmetric modes.

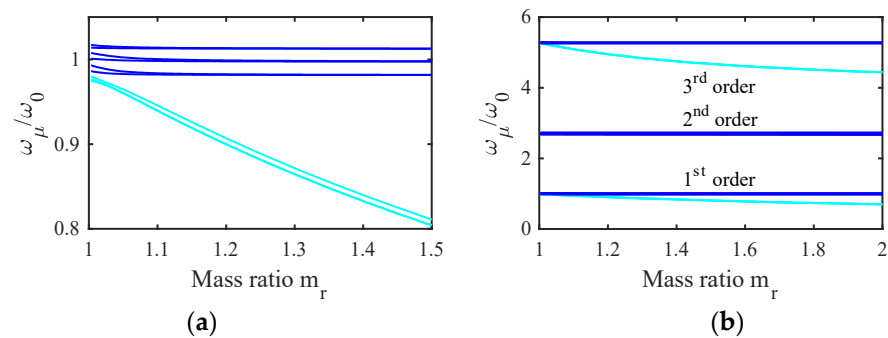


Figure 13. Bank of similar filters: variation of resonant frequencies with m_r for (a) lowest order group and (b) lowest three groups. SMM.

7.4. Filter Banks

Responses predicted by the LEM were verified by the SMM. All were qualitatively identical, so we give only limited examples. Mass ratios m_{r_i} corresponding to those of Figure 11 were obtained by assuming a constant mass width of 22.5 μm and scaling the mass depths appropriately. Array layouts were predictable; for example, Figure 12b shows the deflected shape of an array containing four mass-loaded filters. Figure 14 shows the frequency dependence of transmission for banks of (a) 2, (b) 4, and 8 filters, with beam separations of $s = 8 \mu\text{m}$ (a, b) and $s = 10 \mu\text{m}$ (c). Calculations involved 186, 346, and 666 nodes, respectively, and run times were $\sim 10, 60,$ and 600 s using a 2.6 GHz MacBook Pro, enabling practical exploration of design spaces. This figure should be compared with earlier results from the LEM in Figure 11; there is excellent agreement, confirming that ideal performance can be approached using devices with realizable dimensions.

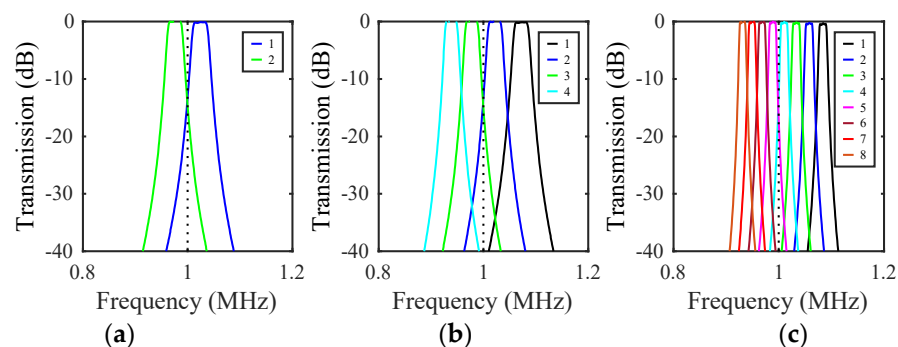


Figure 14. Frequency dependence of transmission for banks of (a) 2, (b) 4, and (c) 8 filters. SMM.

Numerically, we have shown that channel isolation can be improved by raising the number of beams in each array and hence the order of each filter. We have also verified that mode localization and the formation of filter banks can be achieved using third-order modes if the mass ratios, tuning, and matching are modified appropriately. This observation might allow frequencies to be raised without further dimensional reductions.

8. Conclusions

Mass loading has been investigated as a method of forming filter banks based on arrays of coupled beams with parallel plate electrostatic drives. Its effect is to render loaded beams stationary at excitation frequencies within the operating band. For isolated filters, it can provide terminating elements that permit static deflection while suppressing dynamic motion. However, mass loading can also allow intermediate elements to act as reflectors that localize modes to sub-arrays. This principle can be used to develop banks of filters

with different center frequencies for channel selection and multiplexing. The architecture is scalable using simple design rules and the reduction in die size following on from beam sharing improves wafer utilization. Principles have been established using a lumped element model and confirmed using the stiffness matrix method. The main difference is the appearance of higher order modes in the SMM, but similar effects occur at these higher frequency bands and may be exploitable in device applications.

The designs investigated have several performance limitations. The space available for mass-loading elements is small, limiting desynchronization and restricting overall bandwidth. The replacement of built-in beams with cantilevers would allow larger masses to be placed at beam ends. The use of continuous anchors renders any electrostatic tuning global. Although this allows for compensation of global dimensional errors, anchor segmentation would allow for the tuning of individual filters.

There are additional fabrication challenges. The width w_1 of the meander springs must be much less than the width w_0 of the main beams so that the springs are a minor perturbation. The electrode gap g_0 must also be small to avoid unrealistic characteristic impedance. Consequently, nanofabrication will be required to define the layout. Formation of a deep etched structure will then require high sidewall verticality. Connection to internal electrodes might require flip-chip bonding to an electrical backplane.

Some potential solutions exist. The principle is likely applicable to electrostatically coupled resonators, avoiding the problem of fabricating nanoscale features together with nanoscale gaps. The replacement of built-in beams with cantilevers would simplify the connection to electrodes, which may then be accessed from the edge of the array. The principle is also likely to be applicable to torsional resonators, using additional rotary inertia for loading. The coupling elements and electrode gaps will then have nanoscale out-of-plane dimensions, which may be defined as layer thicknesses rather than lithography. The ability to place loading elements above rather than between resonators may also increase achievable loading effects. These alternatives are under investigation.

Author Contributions: Conceptualization, R.S.; methodology, R.S.; software, R.S. and A.B.; validation, R.S. and A.B.; formal analysis, R.S.; investigation, A.B.; writing—original draft preparation, R.S.; writing—review and editing, A.B.; supervision, R.S. All authors have read and agreed to the published version of the manuscript.

Funding: This research received no external funding.

Data Availability Statement: Data are contained within the article.

Acknowledgments: A. Bouchaala is grateful to Imperial College for a PhD studentship.

Conflicts of Interest: The authors declare no conflict of interest.

References

1. Blom, F.R.; Bouwstra, S.; Elwenspoek, M.; Fluitman, J.H.J. Dependence of the quality factor of micromachined silicon beam resonators on pressure and geometry. *J. Vac. Sci. Technol. B* **1992**, *10*, 19–26. [[CrossRef](#)]
2. Alcheikh, N.; Kosuru, L.; Kazmi, S.N.R.; Younis, M.I. In-plane air damping of micro- and nano-mechanical resonators. *J. Micromech. Microeng.* **2020**, *30*, 035007. [[CrossRef](#)]
3. Srikar, V.T.; Senturia, S.D. Thermoelastic damping in fine-grained polysilicon flexural beam resonators. *J. Microelectromech. Syst.* **2002**, *11*, 499–504. [[CrossRef](#)]
4. Duwel, A.; Candler, R.N.; Kenny, T.W.; Verghese, M. Engineering MEMS resonators with low thermoelastic damping. *J. Microelectromech. Syst.* **2006**, *15*, 1437–1445. [[CrossRef](#)]
5. Tang, W.C.; Nguyen, T.-C.H.; Howe, R.T. Laterally driven polysilicon resonant microstructures. *Sens. Actuators* **1989**, *20*, 25–32. [[CrossRef](#)]
6. Nguyen, C.T.-C. Micromechanical resonators for oscillators and filters. In Proceedings of the IEEE Ultrasonics Symposium, Seattle, WA, USA, 7–10 November 1995; pp. 489–499. [[CrossRef](#)]
7. Lin, L.; Howe, R.T.; Pisano, A.P. Micromechanical filters for signal processing. *J. Microelectromech. Syst.* **1998**, *7*, 286–294. [[CrossRef](#)]
8. Wang, K.; Nguyen, C.T.-C. High-order medium frequency micromechanical electronic filters. *J. Microelectromech. Syst.* **1999**, *8*, 534–556. [[CrossRef](#)]

9. Bannon, F.D.; Clark, J.R.; Nguyen, C.T.-C. High-Q HF microelectromechanical filters. *IEEE J. Solid-State Circuits* **2000**, *35*, 512–526. [[CrossRef](#)]
10. Wang, K.; Wong, A.-C.; Nguyen, C.T.-C. VHF free-free beam high-Q micromechanical resonators. *J. Microelectromech. Syst.* **2000**, *9*, 347–360. [[CrossRef](#)]
11. Naghsh Nilchi, J.; Liu, R.; Nguyen, C.T.-C. 7th order sharp-roll-off bridged micromechanical filter. In Proceedings of the 2015 Transducers—2015 18th International Conference on Solid-State Sensors, Actuators and Microsystems (TRANSDUCERS), Anchorage, AK, USA, 21–25 June 2015; pp. 137–140.
12. Nguyen, T.-C. Frequency-selective MEMS for miniaturized low-power communication devices. *IEEE Trans. Micr. Theory Tech.* **1999**, *47*, 1486–1503. [[CrossRef](#)]
13. Li, S.-S.; Lin, Y.-W.; Ren, Z.; Nguyen, C.T.-C. Self-switching vibrating micromechanical filter bank. In Proceedings of the Joint IEEE International Frequency Control/Precision Time and Time Interval Symposium, Vancouver, BC, Canada, 29–31 August 2005. [[CrossRef](#)]
14. Shen, S.-H.; Young, S.-T.; Fang, W. Design and fabrication of a MEMS filter bank for hearing aids applications. In Proceedings of the 2nd Annual IEEE-EMBS Special Topic Conference on Microtechnologies in Medicine and Biology, Madison, WI, USA, 2–4 May 2002. [[CrossRef](#)]
15. Galayko, D.; Kaiser, A.; Legrand, B.; Buchaillet, L.; Combi, C.; Collard, D. Coupled resonator micromechanical filters with voltage tunable bandpass characteristic in thick-film polysilicon technology. *Sens. Actuators A* **2006**, *126*, 227–240. [[CrossRef](#)]
16. Hajhashemi, M.S.; Amini, A.; Bahreyni, B. A micromechanical bandpass filter with adjustable bandwidth and bidirectional control of centre frequency. *Sens. Actuators A* **2012**, *187*, 10–15. [[CrossRef](#)]
17. Manav, M.; Reynen, G.; Sharma, M.; Cretu, E.; Phani, A.S. Ultrasensitive resonant MEMS transducers with tuneable coupling. *J. Micromech. Microeng.* **2014**, *24*, 055005. [[CrossRef](#)]
18. Verbiest, G.J.; Xu, D.; Goldsche, M.; Khodkov, T.; Barzanjeh, S.; von den Driesch, N.; Buca, D.; Stampfer, C. Tunable mechanical coupling between driven microelectromechanical resonators. *Appl. Phys. Lett.* **2016**, *109*, 143507. [[CrossRef](#)]
19. Al Hafiz, M.A.; Kosuru, L.; Hajjaj, Z.Z.; Younis, M.I. Highly tunable narrow bandpass MEMS filter. *IEEE Trans. Electron. Dev.* **2017**, *64*, 3392–3398. [[CrossRef](#)]
20. Galayko, D.; Kaiser, A.; Buchaillet, L.; Collard, D.; Combi, C. Microelectromechanical variable-bandwidth IF frequency filters with tunable electrostatic coupling spring. In Proceedings of the IEEE International Conference on Micro Electro Mechanical Systems, Kyoto, Japan, 19–23 January 2003; pp. 153–156. [[CrossRef](#)]
21. Pourkamali, S.; Ayazi, F. Electrically-coupled MEMS bandpass filters: Part I. *Coupling Elem. Sens. Actuators A* **2005**, *122*, 307–316. [[CrossRef](#)]
22. Ilyas, S.; Chappanda, K.N.; Al Hafiz, M.A.; Ramini, A.; Younis, M.I. An experimental and theoretical investigation of electrostatically coupled cantilever microbeams. *Sens. Actuators A* **2016**, *247*, 368–378. [[CrossRef](#)]
23. Chen, C.-Y.; Li, M.-H.; Chin, C.-H.; Li, S.-S. Implementation of a CMOS-MEMS filter through a mixed electrical and mechanical coupling scheme. *J. Microelectromech. Syst.* **2016**, *25*, 262–274. [[CrossRef](#)]
24. Morankar, A.; Patrikar, R. Dual frequency MEMS resonator through mixed electrical and mechanical coupling. *IET Circuits Devices Syst.* **2018**, *12*, 88–93. [[CrossRef](#)]
25. Abdolvand, R.; Ho, G.K.; Ayazi, F. Poly-wire-coupled single crystal HARPSS micromechanical filters using oxide islands. In Proceedings of the Technical Digest-Solid-State Sensors, Actuators, and Microsystems Workshop, Hilton Head, SC, USA, 6–10 June 2004; pp. 242–245.
26. Arellano, N.; Quévy, E.P.; Provine, J.; Maboudian, R.; Howe, E.T. Silicon nanowire coupled micro-resonators. In Proceedings of the IEEE International Conference on Micro Electro Mechanical Systems, Tucson, AZ, USA, 13–17 January 2008; pp. 721–724. [[CrossRef](#)]
27. Liu, D.; Syms, R.R.A. NEMS by sidewall transfer lithography. *IEEE J. Microelectromech. Syst.* **2014**, *23*, 1366–1373. [[CrossRef](#)]
28. Tasdemir, Z.; Wollschläger, N.; Österle, W.; Leblbici, Y.; Alaca, B.E. A deep etching mechanism for trench-bridging silicon nanowires. *Nanotechnology* **2016**, *27*, 095303. [[CrossRef](#)] [[PubMed](#)]
29. Pourkamali, S.; Hashimura, A.; Abdolvand, R.; Ho, G.K.; Erbil, A.; Ayazi, F. High-Q single crystal silicon HARPSS capacitive beam resonators with self-aligned sub-100-nm transduction gaps. *J. Microelectromech. Syst.* **2003**, *12*, 487–496. [[CrossRef](#)]
30. Kim, H.C.; Chun, K. Photo-assisted electrochemical etching of nano-gap trench with high aspect ratio for MEMS applications. *J. Micromech. Microeng.* **2006**, *16*, 906–913. [[CrossRef](#)]
31. Murakami, S.; Konno, M.; Ikehara, T.; Maeda, R.; Mihara, T. Fabrication of 150-nm-wide transducer gaps for disc-type resonators by single dry etching process. *Jpn. J. Appl. Phys.* **2010**, *49*, 06GN04. [[CrossRef](#)]
32. Lopez, J.; Verd, J.; Uranga, A.; Giner, J.; Murillo, G.; Torres, F.; Abadal, G.; Barniol, N. A CMOS-MEMS RF-tunable bandpass filter based on two high-Q 22-MHz polysilicon clamped-clamped beam resonators. *IEEE Electron. Dev. Lett.* **2009**, *30*, 718–720. [[CrossRef](#)]
33. Chen, C.-Y.; Li, M.-H.; Li, C.-S.; Li, S.-S. Design and characterization of mechanically coupled CMOS-MEMS filters for channel-select applications. *Sens. Actuators A* **2014**, *216*, 394–404. [[CrossRef](#)]
34. Demirci, M.U.; Nguyen, C.T.C. Mechanically corner-coupled square microresonator array for reduced series motional resistance. *J. Microelectromech. Syst.* **2006**, *15*, 1419–1435. [[CrossRef](#)]

35. Chivukula, V.B.; Rhoads, J.F. Microelectromechanical bandpass filters based on cyclic coupling architectures. *J. Sound Vib.* **2010**, *329*, 4313–4332. [[CrossRef](#)]
36. Bouchaala, A.; Syms, R.R.A. New architectures for micromechanical coupled beam array filters. *Microsyst. Technol.* **2020**, *27*, 3377–3387. [[CrossRef](#)]
37. Liu, W.; Chen, Z.; Kan, X.; Wang, T.; Jia, Q.; Zhu, Y.; Zhao, J.; Yuan, Q.; Yang, J.; Yang, F. Novel narrowband radio frequency microelectron-mechanical systems filters. *J. Micromech. Microeng.* **2021**, *31*, 025003. [[CrossRef](#)]
38. Uranga, A.; Verd, J.; Barniol, N. CMOS-MEMS resonators: From devices to applications. *Microelectr. Eng.* **2015**, *132*, 58–73. [[CrossRef](#)]
39. Abdolvand, R.; Bahreyni, B.; Lee, J.R.-Y.; Nabki, F. Micromachined resonators: A review. *Micromachines* **2016**, *7*, 160. [[CrossRef](#)]
40. Syms, R.R.A.; Bouchaala, A. Mechanical synchronization of MEMS electrostatically driven coupled beam filters. *Micromachines* **2021**, *12*, 1191. [[CrossRef](#)]
41. Pierre, C. Mode localization and eigenvalue loci veering phenomena in disordered structures. *J. Sound. Vib.* **1988**, *126*, 485–502. [[CrossRef](#)]
42. Erbes, A.; Thiruvenkatanatan, P.; Woodhouse, J.; Seshia, A.A. Numerical study of the impact of vibration localization on the motional resistance of weakly coupled MEMS resonators. *J. Microelectromech. Syst.* **2015**, *24*, 997–1005. [[CrossRef](#)]
43. Thomson, W.T. *Theory of Vibration with Applications*, 4th ed.; Prentice Hall: Englewood Cliffs, NJ, USA, 1993. [[CrossRef](#)]
44. de Irassar, P.L.V.; Ficcadenti, G.M.; Laura, P.A.A. Dynamic analysis of a beam with an intermediate elastic support. *J. Sound Vib.* **1984**, *96*, 381–398. [[CrossRef](#)]
45. Osterberg, P.M.; Senturia, S.D. M-TEST: A test chip for MEMS material property measurement using electrostatically actuated test structures. *J. Microelectromech. Syst.* **1997**, *6*, 107–118. [[CrossRef](#)]
46. Hopcroft, M.A.; Nix, W.D.; Kenny, T.W. What is the Young’s modulus of silicon? *J. Microelectromech. Syst.* **2010**, *19*, 229–238. [[CrossRef](#)]
47. Zienkiewicz, O.C.; Taylor, R.L.; Zhu, J.Z. *The Finite Element Method: Its Basis and Fundamentals*; Butterworth Heinemann: Oxford, UK, 2013. [[CrossRef](#)]
48. McGuire, W.; Gallagher, R.H.; Ziemian, R.D. *Matrix Structural Analysis*, 2nd ed.; John Wiley: New York, NY, USA, 2000. [[CrossRef](#)]
49. Hung, E.S.; Senturia, S.D. Generating efficient dynamical models for microelectromechanical systems from a few finite-element simulation runs. *J. Microelectromech. Syst.* **1999**, *8*, 280–289. [[CrossRef](#)]
50. Clark, J.V.; Zhou, N.; Pister, K.S.J. MEMS Simulation Using SUGAR v0.5. In Proceedings of the Technical Digest-Solid-State Sensors, Actuators, and Microsystems Workshop, Hilton Head, SC, USA, 8–11 June 1998; pp. 191–196.

Disclaimer/Publisher’s Note: The statements, opinions and data contained in all publications are solely those of the individual author(s) and contributor(s) and not of MDPI and/or the editor(s). MDPI and/or the editor(s) disclaim responsibility for any injury to people or property resulting from any ideas, methods, instructions or products referred to in the content.